JOURNAL OF PROPULSION AND POWER
Vol. 23, No. 6, November–December 2007

Hypersonic Inlet Studies for a Small-Scale Rocket-Based Combined-Cycle Engine

Giulio Riva,* Adolfo Reggiori,† and Giambattista Daminelli‡
Consiglio Nazionale delle Ricerche - Istituto per l' ENergetica e le Interfasi–Milano, 20125 Milano, Italy

DOI: 10.2514/1.29845

Experimental tests on a small-scale rocket-based combined-cycle model engine at Mach 8 were conducted to investigate the influence of inlet airflow changes on the engine performance. Flat plates of different lengths with a sharp leading edge and parallel to the freestream airflow, simulating the presence of vehicle body, were mounted before the inlet bottom surface. The test results indicated that fuel ignition, combustion chamber pressure, and engine net thrust were strongly affected by moderate changes of the flat plate length. The formation of an oblique shock wave due to hypersonic viscous interaction effects was observed above the flat plates. External compression of the captured airflow and lateral mass spillage were quantified on the basis of wall pressure measurements near the engine inlet for all tested plates. A convenient flat plate length range was identified that minimized spillage and optimized the engine performance.

Nomenclature

A	=	area, m^2
h	=	height, m
l	=	length, m
M	=	Mach number
$\dot{m}$	=	mass flow rate, kg/s
p	=	pressure, Pa
R	=	gas constant, J/(kg · K)
T	=	temperature, K
v	=	velocity, m/s
x	=	abscissa, m
z	=	width, m
β	=	oblique wave angle, deg
γ	=	specific heat ratio
δ	=	boundary layer angle, deg
ρ	=	density, kg/m^3

Subscripts

a	=	subsonic (boundary layer) inlet region
b	=	supersonic inlet region
c	=	hypersonic inlet region
capt	=	capture
e	=	flat plate lateral edges
$f-s$	=	freestream
H2	=	hydrogen
i	=	inlet
max	=	maximum
p	=	flat plate
pitot	=	pitot
SUB	=	subsonic region, lateral surface
SUPER	=	supersonic region, lateral surface
tot	=	total or stagnation
x	=	freestream direction
∞	=	freestream value

Received 18 January 2007; revision received 24 May 2007; accepted for publication 8 June 2007.

*Research Scientist, via Cozzi 53, riva@ieni.cnr.it.
†Associate Research Scientist; Professor, Department of Mechanical Engineering; currently at University of Brescia, Brescia, Italy; reggiori@ieni.cnr.it.
‡Senior Technician, via Cozzi 53; daminelli@ieni.cnr.it.

I. Introduction

ROCKET-BASED combined-cycle (RBCC) propulsion systems are among the possible options for powering the future generation of reusable launchers, as they offer a possibility for lowering the cost of launching payloads into Earth orbit. Considerable efforts have been made during the last 15 years to develop reliable design tools for these launchers and experimental work on model engines and prototypes has been performed [1–7]. These engines combine the advantages of rocket and airbreathing propulsion, and change their operation mode as the flight speed progressively increases. In particular, they are intended to work in rocket-ejector mode up to Mach 3 to 4, ramjet mode up to Mach 5 to 6, and scramjet mode up to Mach 12 to 15 [1–3]. Finally, for higher flight speeds and altitudes above 40–45 km, the pure rocket mode should be adopted. As a matter of fact, they are intended to operate as airbreathing engines for most of the atmospheric flight, covering flight speeds that range from subsonic to high hypersonic regimes.

The hypersonic flight is characterized by peculiar phenomena associated with the intense aerodynamic heating of the air when its relative speed is decreased, as in boundary layers and engine compression components [8,9]. Viscous dissipation in hypersonic boundary layers produces strong temperature increments that increase the viscosity coefficient, and this by itself makes the boundary layer thicker. In particular, hypersonic viscous interaction is a mechanism that intensifies the influence of boundary layers on the nature of outer inviscid flow, whose changes feed back as modifications of the boundary layer structure [9]. These effects may modify the angle of compression surfaces as far as the outer inviscid flow is concerned or may create fluid compression ramps above surfaces parallel to the freestream flow direction.

A typical example of viscous interaction is the flow pattern above a flat plate with a sharp leading edge immersed in a parallel hypersonic flow. Inviscid flow would not produce any pressure increment on the flat plate and would remain unperturbed. On the contrary, for viscous flows, a rapidly growing boundary layer and a shock wave establish above the flat plate with wall pressure much higher than the freestream value and a pressure distribution featuring a maximum near the plate leading edge [9]. This fact may lead to macroscopic effects on the inlet of hypersonic airbreathing engines as they are often designed for using the vehicle body to perform a preliminary external compression of the captured air. It is obvious that a thick

boundary layer may significantly affect the inlet flow pattern, with consequences in terms of engine overall thrust and efficiency.

Recent experimental studies based on parametric changes of inlet components of combined-cycle or scramjet engines demonstrated how the inlet geometry may be critical for the overall engine performance. In particular, the influence on the inlet flow compression of cowl length and angle [10] and internal strut geometry [11] was investigated for Mach 4 simulated flight speed. Substantial inlet geometry changes may also be required to limit base drag and stabilize the flame position as the flight speed increases [12] and viscous interaction becomes more relevant.

Some effects of hypersonic viscous interaction on the performance of a small-scale RBCC engine are investigated in this paper. For this purpose an engine setup featuring a replaceable flat plate just upstream of the inlet bottom surface was built, and a number of tests at Mach 8 simulated flight velocity based on the parametric change of the plate length were conducted in the CNR-IENI pulsed hypersonic tunnel [13].

II. RBCC Model Setup

The model length is approximately 600 mm, with a rectangular shape of the internal channels. The inlet size is 40 mm in height and 100 mm in width. The internal compression surfaces shrink the channels cross-sectional area by decreasing the width, while the height remains unchanged along the entire model. A sketch of the internal geometry of the engine is given in Fig. 1, where the flat plate upstream of the bottom surface and the locations of pressure and temperature sensors are also shown. The model is equipped with a small size rocket engine fed with gaseous hydrogen and oxygen that can be operated in three different modes:

1) a rocket, providing high temperature hydrogen/water mixtures (1000–1500 K);

2) an injector of cold H_2/O_2 mixtures;

3) an injector of cold hydrogen.

The fuel (or fuel rich mixture) injection is always parallel to the airflow direction, thus contributing to the engine thrust. In all cases the working conditions can significantly be varied, and values of the overall equivalence ratio (ER) in the range 0.5–1.2 can be explored.

Several engine geometries were found that provided high combustion efficiency over a wide ER range and, for these geometries, positive net thrust was produced for ER approaching unity. The model engine performance was found to be strongly dependent on apparently small changes of the inlet geometry (i.e., flat plate length). The inlet flow was thus studied in detail, attempting to understand the reasons of such a big influence and to describe with reasonable approximation the airflow pattern actually captured by the engine inlet. The location of the flat plate with sharp leading edge upstream of the model bottom surface is indicated by the perspective view in Fig. 2. No gap was left between the plate and the engine inlet.

The initial purpose was a parametric change of both flat plate length and angle with respect to the freestream direction, in such a way as to provide different intensities of the airflow external compression as well as different capture areas. Preliminary tests at Mach 8 showed, however, that, even without providing any compression angle, the simple change of the flat plate length produced macroscopic changes of the engine performance that ranged from the failure of fuel ignition (long plate) to the inlet blockage with the formation of a normal shock wave before the inlet (plate removed), a situation known as "pitot" inlet [14]. It was thus decided to investigate in detail the influence of the plate length with zero geometrical compression angle, which also means no changes of the freestream capture area. All tests were conducted at Mach 8 nominal flight velocity.

III. Inlet Physical Model

The presence of a flat plate with a sharp leading edge parallel to the airflow just upstream of the inlet section as shown in the perspective view of Fig. 2 should produce, for a perfectly parallel flow of a nonviscous gas, a Mach wave on the upper side of the plate that

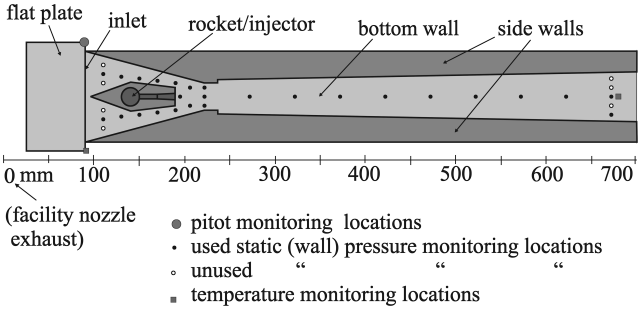

Fig. 1 Schematic of the RBCC model internal channel geometry.

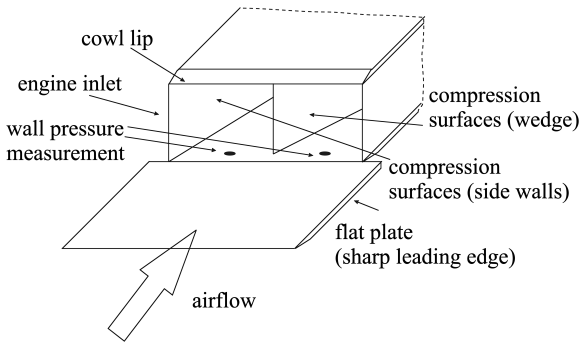

Fig. 2 Perspective view of the engine inlet (qualitative sketch).

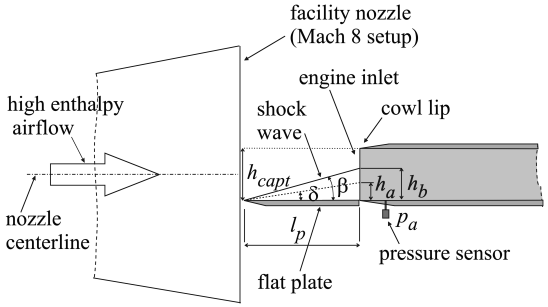

Fig. 3 Side view of the model shown in Fig. 2 with the pressure monitoring location near the inlet section. A qualitative sketch of the flow pattern before the inlet is also indicated.

leaves the captured airflow unperturbed. The actual experimental conditions established in the test chamber are far from this ideal situation for the following reasons:

1) The airflow is not parallel as it is produced by a conical nozzle with a total divergence angle of 20 deg. Although the model is mounted on the nozzle centerline and its size is much smaller than the nozzle exit diameter, a 2–3 deg compression angle should be considered for a plate aligned with the bottom wall.

2) The airflow features high stagnation enthalpy, of the order of 2 MJ/kg. This means that in the boundary layer the temperature may be of the order of 2000 K, with a consequent strong increment of the viscosity that makes the boundary layer itself grow faster. Moreover, some dissociation phenomena may occur. This situation is known in hypersonic aerodynamics as "viscous interaction."

3) The Reynolds number in these tests is relatively low (about 1.5×10^6 m^{-1}), with characteristic lengths of the order of 0.1 m. Under these conditions, the boundary layer, being probably of laminar type, is thicker and may cause stronger perturbation in the captured airflow [14].

The formation of a boundary layer of relevant and rapidly growing thickness suggests the idea that the entire flow swallowed by the engine could be strongly modified with respect to the nominal freestream conditions. To quantify this presumed modification, the wall static pressure was measured at the axial location shown in

Fig. 3. The same monitoring locations are also visible in Figs. 1 and 2.

The wall pressure at the indicated monitoring location is not affected by the internal compression surfaces because it is sufficiently far from either the central structure or the side walls. The only possible influence may come from the flow above the upstream flat plate.

In all tests the wall pressure p_a was found to be considerably higher than the freestream static pressure, featuring values compatible with the formation of an oblique shock wave at the leading edge of the flat plate. Because both pressure ratio across the shock wave and freestream Mach number are known, the wave angle with respect to the freestream direction can be computed from oblique shock theory [15].

$$\sin\beta = \left[\frac{\gamma - 1 + (\gamma+1)p_a/p_\infty}{2\gamma M_\infty^2}\right]^{\frac{1}{2}} \tag{1}$$

The oblique shock wave, however, is not produced by any solid compression surface, as the flat plate is nearly parallel to the freestream direction and the small angle due to the conical shape of the facility nozzle cannot justify the observed pressure increment. The wave may thus be the consequence of a rapidly growing boundary layer, which can be considered as a fluid wedge of low speed flow characterized by high static temperature and low density. The fluid wedge angle is given by the following equation:

$$\tan\delta = \cot\beta \frac{M_\infty^2 \sin^2\beta - 1}{[(\gamma+1)/2]M_\infty^2 - (M_\infty^2 \sin^2\beta - 1)} \tag{2}$$

The oblique shock equations also provide the shock wave downstream Mach number:

$$M_b^2 = \frac{(\gamma-1)M_\infty^2 \sin^2\beta + 2}{2\gamma M_\infty^2 \sin^2\beta - (\gamma-1)} \csc^2(\beta - \delta) \tag{3}$$

In accordance with this model (Fig. 4), the airflow above the flat plate is characterized by three regions:

1) a low speed, high temperature region that gives a small contribution to the captured mass flow rate;

2) a supersonic region with air compressed by the oblique shock wave;

3) a hypersonic region of unperturbed freestream flow.

The intersections of these regions with the engine inlet define three surfaces whose area can be computed on the ground of the above defined quantities:

$$A_a \equiv z_i h_a = z_i l_p \tan\delta \tag{4}$$

$$A_b \equiv z_i (h_b - h_a) = z_i l_p (\tan\beta - \tan\delta) \tag{5}$$

$$A_c \equiv z_i (h_{\text{capt}} - h_b) = z_i (h_{\text{capt}} - l_p \tan\beta) \tag{6}$$

This model clearly simplifies the actual flow structure produced by viscous interaction as the boundary layer thickness is assumed to grow linearly and pressure is considered constant along the plate. According to the results of accurate viscous interaction studies [9,14], the static pressure increases near the plate leading edge, where the boundary layer thickness also grows faster (strong viscous interaction). Such a detailed description is, however, beyond the purpose of this work and would require a much more detailed wall pressure monitoring system.

The transversal pressure gradient (p_a on the flat plate centerline and p_∞ on the side edges) can produce spillage of a portion of the airflow outside the model side walls. A method for quantifying the lateral spillage is based on the momentum balance of the airflow compressed by the shock wave along the transversal direction (subsonic and supersonic regions in Fig. 4). The evaluation of the

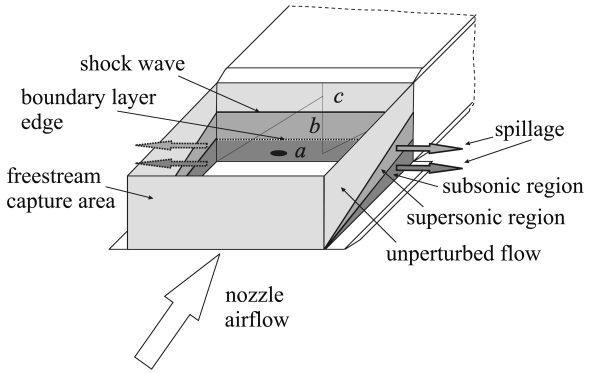

Fig. 4 Perspective view of the flow pattern above the flat plate.

lateral spillage by means of the momentum equation is based on the following assumptions:

1) Subsonic and supersonic regions only contribute to the spillage; the unperturbed flow region gives no contribution as there is no pressure gradient.

2) The pressure is assumed uniform in both subsonic and supersonic regions, with the exception of a layer near the flat plate lateral edges bounded by the Mach lines departing from the plate upstream corners, in which the pressure drops to the freestream value.

3) The temperature in the supersonic region is that provided by the oblique wave equations.

4) The temperature in the subsonic region (boundary layer) is the stagnation temperature.

For symmetry reasons, on the flat plate centerline the transversal velocity is zero; thus the momentum equation per unit area applied to a domain bounded by the plate centerline and lateral edge is

$$p_a = p_\infty + \rho_e v_e^2 \tag{7}$$

The transversal flow velocity is thus

$$v_e = \sqrt{\frac{p_a - p_\infty}{\rho_e}} \tag{8}$$

The total transversal mass flow rate (or total spillage) calculation must consider the contributions of both subsonic and supersonic regions behind the oblique wave on both sides of the flat plate:

$$\dot{m}_e = 2[(\rho_e v_e A_e)_{\text{SUB}} + (\rho_e v_e A_e)_{\text{SUPER}}] \tag{9}$$

For the subsonic region:

$$\rho_e = \frac{p_\infty}{RT_{\text{tot}}} \tag{10}$$

$$A_e = \frac{l_p^2 \tan\delta}{2} \tag{11}$$

$$(\rho_e v_e A_e)_{\text{SUB}} = \frac{1}{2} l_p^2 \tan\delta \sqrt{\frac{p_\infty}{RT_{\text{tot}}}(p_a - p_\infty)} \tag{12}$$

For the supersonic region:

$$\rho_e = \frac{p_\infty}{RT_b} \tag{13}$$

$$A_e = \frac{l_p^2 (\tan\beta - \tan\delta)}{2} \tag{14}$$

$$(\rho_e v_e A_e)_{\text{SUPER}} = \frac{1}{2} l_p^2 (\tan\beta - \tan\delta) \sqrt{\frac{p_\infty}{RT_b}(p_a - p_\infty)} \tag{15}$$

The total lateral mass spillage is thus

$$\dot{m}_e = l_p^2 \sqrt{\frac{p_\infty}{R}(p_a - p_\infty)}\left[\tan\delta\sqrt{\frac{1}{T_{\text{tot}}}} + (\tan\beta - \tan\delta)\sqrt{\frac{1}{T_b}}\right] \quad (16)$$

An empirical correction factor should be applied to Eq. (16) when the flat plate transversal size is larger than the corresponding inlet size. For a flat plate much larger than the inlet, the flow on the plate edges has small influence on the flow near the model side walls and thus the spillage becomes negligible. On the contrary, when the plate and the inlet feature the same width, the mass spillage must be fully considered. In this case the plate width was 120 mm with an inlet width of 100 mm. The flat plate lateral edges were thus 10 mm external with respect to the inlet side walls. For such a geometry an empirical correction factor 5/6 was applied to the side mass spillage [Eq. (16)].

The calculation of the mass flow rates for the three inlet regions is now detailed. The mass flow rate through the freestream capture area is

$$\dot{m}_{f-s} = \rho_\infty v_\infty A_{\text{capt}} \quad (17)$$

The mass flow rate actually captured by the engine inlet is evaluated as the sum of several contributions (see Fig. 4):

$$\dot{m} = \dot{m}_a + \dot{m}_b + \dot{m}_c \quad (18)$$

where:

$$\dot{m}_a = 0 \quad (19)$$

$$\dot{m}_b = \rho_b v_b \cos\delta A_b - 5/6\dot{m}_e \quad (20)$$

$$\dot{m}_c = \rho_\infty v_\infty A_c \quad (21)$$

Region *a* (corresponding to the boundary layer) is assumed to give no contribution to the overall mass flow rate; however, the air flowing in this region is part of that compressed by the oblique wave and is thus attributed to region *b*. The following correlation also holds:

$$\dot{m}_{f-s} = \dot{m} + 5/6\dot{m}_e \quad (22)$$

IV. Experimental Tests

A number of experimental tests at Mach 8 simulated flight speed were conducted to define the flat plate length range suitable for this study. In all cases the test flow was vitiated air (20% water content in volume) whose total enthalpy was increased by a combination of rapid compression and hydrogen precombustion [13]. Although the hypersonic flow total duration was approximately 200 ms (starting from about 170 ms after the acquisition trigger), the actual test time interval was limited to 50 ms, in which the freestream dynamic pressure decreased from 2 to 1.5×10^4 Pa and the Reynolds number was about 1.5×10^6 m^{-1}. In a typical test, pressure was detected at 10 locations to control and monitor the correct operation of the tunnel. These monitoring locations include all components of the pulse facility: free-piston compressor, stagnation vessel, nozzle, rocket/injector fueling system, and test chamber. Pressure levels range from 20–30 MPa (free-piston compressor pump tube) to 50 Pa (test chamber). The RBCC model (Fig. 1) was equipped with 26 static pressure sensors, all mounted on the bottom wall along the internal channels, pitot and temperature probes near the engine inlet, and temperature probe at the engine exhaust. Piezoresistive transducers with the appropriate full scale value, 100 kHz (or higher) natural frequency, 1% (or less) global accuracy, were used for transient pressure measurements. A capacitive transducer, 1 kPa full scale was employed for static pressure measurements in the test chamber, which was embodied in a 22 m^3 volume dump tank. The test gas stagnation temperature was evaluated at the engine inlet and exhaust by measuring the electrical resistance change of a 80 μm diam, 25 mm length iridium wire, that was found to be sufficiently robust to withstand the mechanical and thermal loads of the Mach 8 simulated flight conditions and of the engine exhaust gas flow. The data acquisition system was based on a 12 bit, 10 V full scale, 40 channels (five 8 channel boards) acquisition system. Each board has a maximum overall sampling frequency of 1.25 MHz. The actual sampling frequency for each monitoring location was 50 kHz.

All tests reported in this paper were conducted without replacing or modifying any components or sensors of the model engine, leaving aside the flat plate before the inlet whose length was parametrically changed in the range 60–80 mm. Preliminary results showed that plate lengths of 60 mm or lower were characterized by a much higher pressure at the engine inlet. In these cases subsonic flow was established inside the engine compressor, with the formation of a strong oblique wave above the flat plate that compressed nearly all captured air. Flat plate lengths of 65 mm or higher allowed a correct inlet start with the formation of a weaker shock wave. The wave characteristics were computed on the basis of the measured wall pressure near the engine inlet (that is, immediately downstream of the plate trailing edge). As detailed in the previous section all wave characteristics can be computed once the freestream flow conditions and the wave downstream pressure are known. Four values of the flat plate lengths were considered in this study:

1) $l_p = 65$ mm (setup CR1MD22, eight tests);
2) $l_p = 70$ mm (setup CR1MD19, seven tests);
3) $l_p = 75$ mm (setup CR1MD21, five tests);
4) $l_p = 80$ mm (setup CR1MD20b, four tests).

Some data concerning the 60 mm length plate will also be given to emphasize the different behavior of such a setup. Although the nominal freestream Mach number was 8 in all cases, the actual Mach number was computed for each test on the basis of the facility nozzle upstream stagnation pressure and the engine inlet pitot pressure, with the assumption of isentropic nozzle flow. Average values over the time interval from 200 to 250 ms from the acquisition trigger were considered, corresponding to the freestream thermodynamic properties that better simulate the flight conditions. All Mach number data fall within the range from 7.6 to 7.9. The inlet wall pressure referring to the pitot pressure of the freestream flow is shown in Fig. 5 as a function of the freestream Mach number.

Shorter plates produce higher pressure, in agreement with the known viscous interaction effects, as the monitoring location is closer to the leading edge. These pressure data were used to compute the oblique wave angle, in accordance with Eq. (1), in which the specific heats ratio γ is approximately 1.33, as computed on the basis of the airflow composition (vitiated air with 20% water volume) and temperature. The wave angles, given in Fig. 6, show values in the range of 17.5–19.6 deg.

The formation of an oblique shock wave was confirmed by the visualization of the flowfield above the flat plate. Several time-resolved images (1 ms) using both schlieren and shadow optical

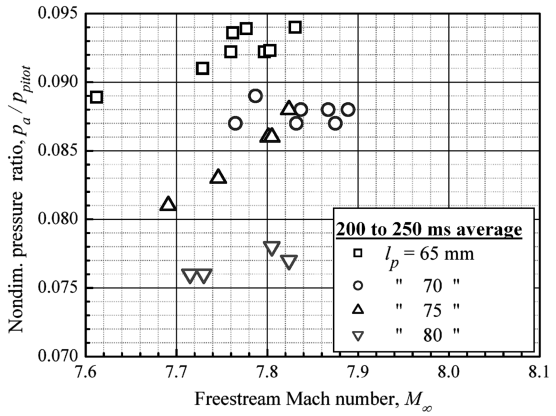

Fig. 5 Nondimensional wall pressure at the engine inlet. Different plate lengths are indicated with different symbols.

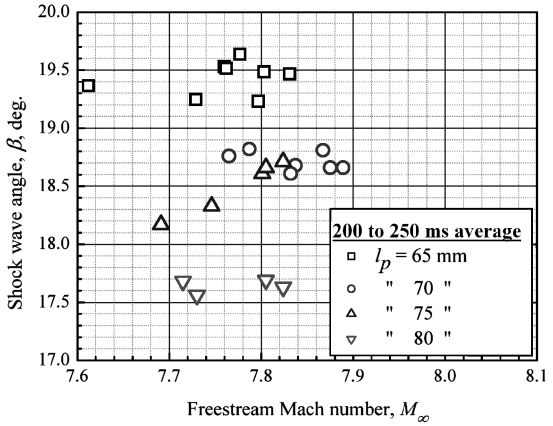

Fig. 6 Oblique shock wave angle for different flat plate lengths.

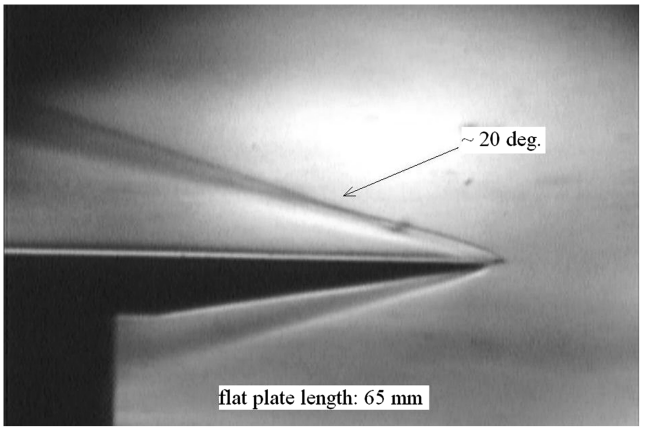

Fig. 7 Schlieren image of the flowfield above the flat plate.

configurations showed the presence of an oblique shock wave departing from the flat plate leading edge with angles compatible with those computed according to Eq. (1) and reported in Fig. 6. All images were taken for the 65 mm plate length using a charge-coupled device (CCD) camera working at 50 fps with 1 ms exposition time for each frame. A typical schlieren image taken from these sequences is given in Fig. 7, where a wave angle of about 20 deg can be observed, in good agreement with the computed values.

The formation of the oblique wave was thus proved and its angle correctly predicted. The fluid wedge angle (i.e., boundary layer angle) that originates the wave can be evaluated according to Eq. (2), in such a way as to define all regions of the flowfield above the flat plate and characterize with sufficient detail the airflow captured by the engine inlet. A map of the fluid wedge angles is given in Fig. 8 that substantially duplicates the pattern of the wave angles but with values about 5.5 deg smaller.

The oblique shock theory provides all flow properties downstream of the wave, including Mach number, temperature, and density. In particular, the Mach number decreases from 8 (freestream) to 5 and the static temperature doubles with respect to the freestream value. The lateral spilled mass flow rate was computed according to Eq. (16), multiplied by an empirical factor 5/6 to account for the fact that the flat plate is wider than the engine inlet, and expressed as a fraction of the mass flow rate passing through the geometric freestream capture area of the engine.

The results shown in Fig. 9 indicate that the short plates produce less spillage. The spilled mass ranges from 3.7% of the 65 mm plate to the 4.7% of the 80 mm plate. As will be shown next, such a small difference in the air mass flow rate swallowed by the engine (1%) contributes to modify substantially the engine performance.

Another effect of plate length changes is related to the fraction of the captured airflow compressed by the oblique shock before the engine inlet. The precompressed air mass flow rate [Eq. (20)] was

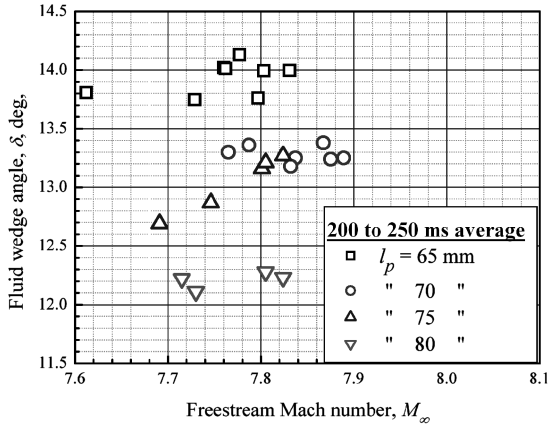

Fig. 8 Fluid wedge (i.e., boundary layer) angle for different flat plate lengths.

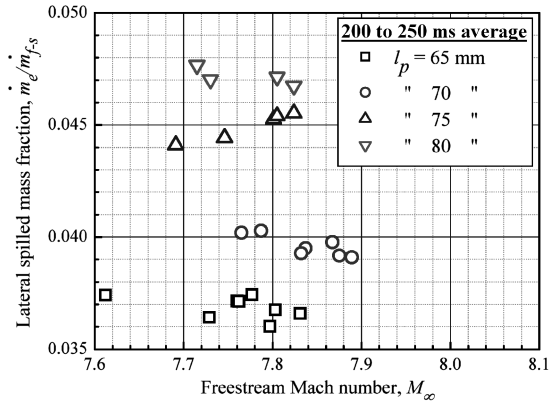

Fig. 9 Lateral spilled mass fractions for different flat plate lengths.

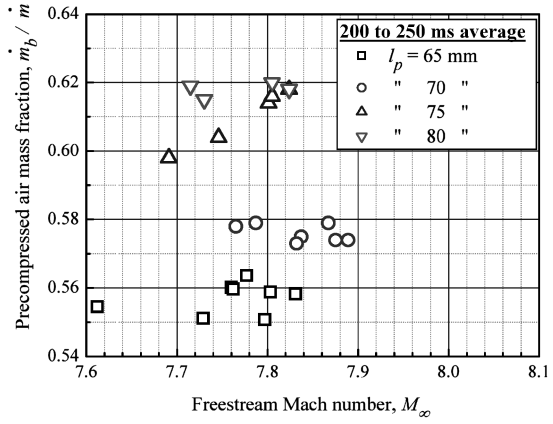

Fig. 10 Precompressed air mass fractions for different flat plate lengths.

normalized with the total captured air mass flow rate [Eq. (18)] and average values over the time interval from 200 to 250 ms were considered for each test. The results, given in Fig. 10, reveal that in all cases more than one-half of the captured air is compressed before the engine inlet, with values ranging from about 55% of the shorter plate (65 mm) to 62% of the 80 mm plate.

Both spillage and precompression changes contribute to substantially modify the engine efficiency. Pressure data taken from all monitoring locations along the flowpath inside the engine (Fig. 1) give a clear indication of the plate length influence. To make all cases comparable, pressure data were referred to the freestream pitot pressure and averaged over the time interval 200–250 ms. For all

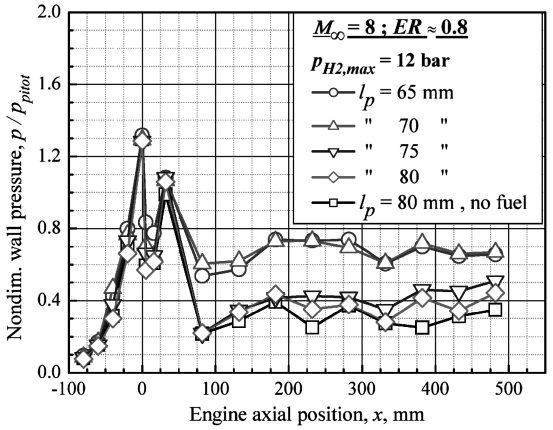

Fig. 11 Nondimensional pressure distribution along the engine internal flowpath for different flat plate lengths and identical fuel injection conditions.

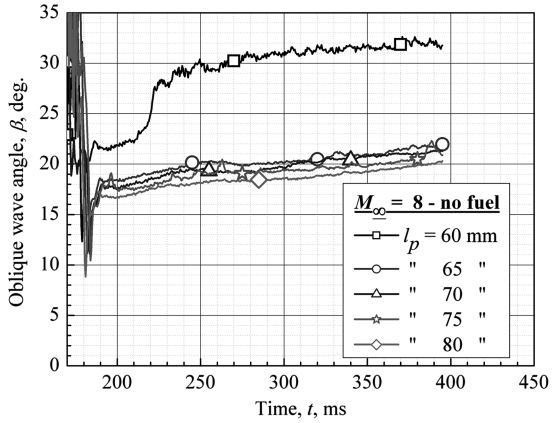

Fig. 13 Time evolution of the shock wave angle for different flat plate lengths, showing the different behavior of the setup with the shorter plate.

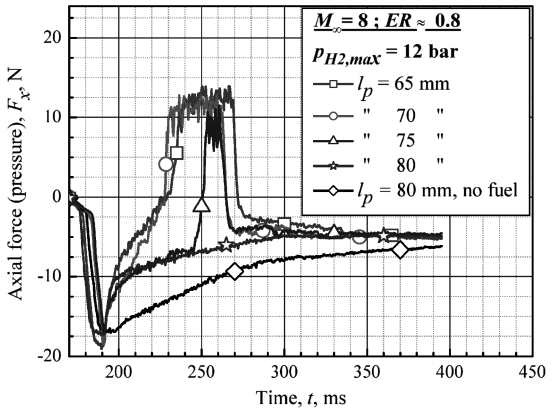

Fig. 12 Axial force computed from pressure data along the engine internal flowpath for different flat plate lengths and identical fuel injection conditions.

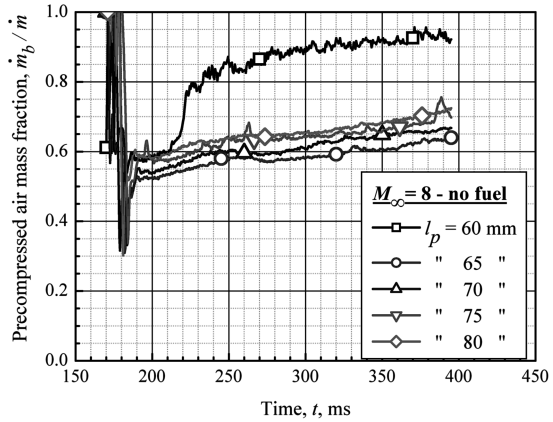

Fig. 14 Time evolution of the precompressed air mass fraction for different flat plate lengths, showing the different behavior of the setup with the shorter plate.

geometries (i.e., flat plate lengths) the same fuel injection condition was adopted [room temperature hydrogen, 12 bar (1.2 MPa) maximum injection pressure, corresponding to an overall equivalence ratio of about 0.8]. The axial pressure distribution along the engine (compressor, injection chamber, combustion chamber) is given in Fig. 11 for the different flat plate lengths. For axial locations with more than one pressure probe (Fig. 1), the average value was considered.

The pressure distribution without fuel injection is given as a reference case for the 80 mm plate only, being nearly independent from the flat plate length. It must be remarked that along the compressor (negative x values in Fig. 11) the pressure distribution is approximately the same in all cases, while the different levels downstream of the injection location ($x = 0$) indicate different combustion efficiencies (higher for the shorter plates).

The calculation of the net axial force produced by the internal pressure can immediately be performed as the internal engine geometry is known (Fig. 1). The time evolution of such a force, which is the most important component of the net thrust, is given in Fig. 12 for all geometries. An unfueled test is also given as reference. The data in Fig. 12 indicate increasing forces and longer combustion times for decreasing flat plate lengths. It is also possible to discriminate the effect of mass injection (axial in all cases) by comparing the unfueled case with the corresponding case (80 mm plate) in which the fuel is injected but not burned. Fuel injection starts approximately at 190 ms. The additional force produced by the combustion process for the shorter plates is also evident.

The reduction of the flat plate length to 60 mm produces a dramatic change of the inlet conditions that are synthesized in Fig. 13, where the time evolutions of the oblique wave angles above the plate are compared. It can clearly be seen that, for lengths of 65 mm or above, all curves are grouped in a narrow range around 20 deg, while the 60 mm case features angles 5–10 deg higher.

Under these conditions, the wave is still swallowed by the engine inlet, but most of the air captured is precompressed to a lower Mach number. The fraction of precompressed air also increases significantly up to 80–90% of the captured flow, as shown in Fig. 14.

The test analysis provides the distribution of the captured air mass flow rate on the different regions of the inlet section as defined in Fig. 4. Region *a* corresponds to the boundary layer, which is considered a fluid wedge providing a negligible contribution to the overall air capture process: the air flowing in this region is, however, part of that compressed by the oblique wave and attributed to region *b*. Region *c* captures the remaining unperturbed portion of the flow coming from the freestream capture area. The captured air mass flow rate distribution over the different regions for both 60 and 65 mm plate lengths is shown in Figs. 15 and 16. The lateral spillage is represented by the difference between the air mass flow rate crossing the freestream capture area and the air mass flow rate actually captured.

The main intake fluid dynamic variables for flat plate lengths from 60 to 80 mm are summarized in Figs. 17 and 18. Again, time averaged values in the range 200–250 ms were considered and a further average on the test cases with the same geometry was performed.

Pressure, shock wave angle, and boundary layer angle monotonically increase as the flat plate length decreases, while spilled and precompressed air feature a minimum for the 65 mm plate. A change of the inlet behavior is clearly observable for the 60 mm plate length.

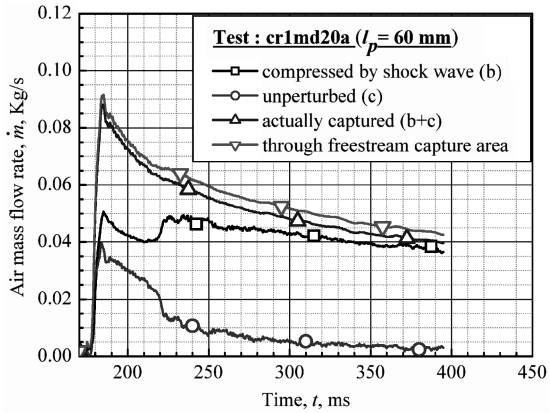

Fig. 15 Mass flow rate distribution for plate length of 60 mm.

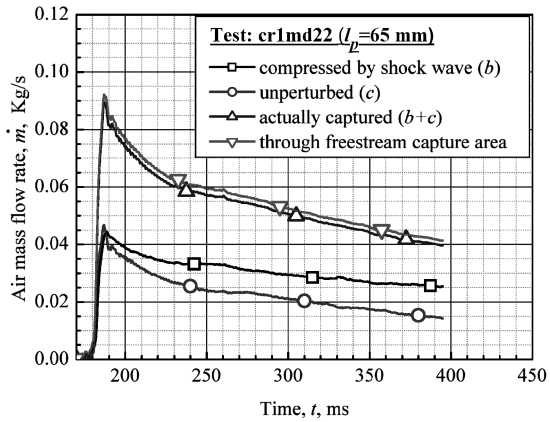

Fig. 16 Mass flow rate distribution for plate length of 65 mm.

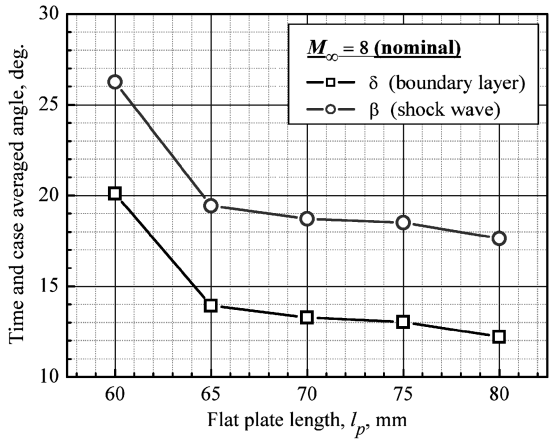

Fig. 17 Influence of the flat plate length on the boundary layer and oblique shock wave angles.

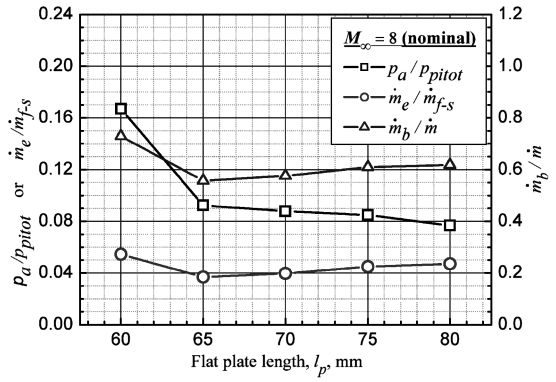

Fig. 18 Influence of the flat plate length on inlet pressure, lateral spillage, and fraction of precompressed air.

The observed effects on the engine operation of plate length changes may be connected with the corresponding changes of the engine inlet conditions. The longer plates feature higher precompressed mass fractions and higher spillage (i.e., less captured air mass). This means that a lower amount of air at a lower average speed is compressed by the engine inlet, whose contraction ratio (constant for all plate lengths) provides lower pressure and temperature increments. This may be sufficient to increase ignition delays to values incompatible with the combustor length. Shorter plates increase average speed and mass of the captured airflow, making the internal compression surfaces capable of providing a sufficient temperature recovery and thus a sufficiently short ignition delay. For plates shorter than a given threshold (60 mm or less), inlet blockage occurs as the amount of the captured flow is excessive and its average speed is too high for the given inlet contraction ratio [16].

V. Conclusions

Inlet flow studies on a small-scale RBCC model engine at Mach 8 simulated flight velocity revealed that the presence of a flat plate parallel to the airflow before the engine bottom wall originates a complex 3-D fluid dynamic field that affects significantly the engine performance. Viscous interaction effects typical of hypersonic flight were clearly detected and resulted in the formation of an oblique shock wave, despite the absence of geometrical compression angles that could justify a shock of the observed strength. As a consequence, a stratified flow was produced on the inlet section, consisting of subsonic (boundary layer), supersonic, and hypersonic regions. A relevant portion of the captured air is thus precompressed by the oblique wave and lateral spillage from the subsonic and supersonic regions takes place. Parametric studies on the effects of the flat plate length indicated a threshold size below which the shock wave increases its strength and induces blockage of the engine inlet. For the tested engine, the optimum flat plate length was found to be in the range of 65–70 mm, whereas, for values higher than 75 mm, combustion was not sustained and no positive thrust was provided. For optimum geometries, both lateral spillage and precompressed air mass fraction are minimized and engine combustion efficiency and thrust are optimized. It may be inferred that plate lengths within the optimum range produce the best average inlet flow conditions for the given internal contraction ratio, allowing higher compression and temperature increments of the captured air and making ignition delays shorter than flow residence times in the combustion chamber. External compression and spillage can thus be governed by this simple technique that could be used to "tune" the engine performance for different flight conditions without changing the internal geometry and with small changes of the overall aerodynamic drag. On the other hand, if not adequately understood, viscous effects on the inlet flow may be a severe problem that can affect the overall performance of hypersonic airbreathing engines and limit their operation range.

Acknowledgments

This research was funded by the National Research Council (CNR), RSTL-808. The Italian Space Agency (ASI) contributed to the development of the Consiglio Nazionale delle Ricerche - Istituto per l' ENergetica e le Interfasi (CNR-IENI) hypersonic facility (Contract No. I/R/252/02/0).

References

[1] Olds, J., and Walberg, G., "Multidisciplinary Design of a Rocket-Based Combined Cycle SSTO Launch Vehicle Using Taguchi Methods," AIAA Paper 93-1096, Feb. 1993.

[2] Olds, J., "Results of a Rocket-Based Combined Cycle SSTO Design Using Parametric MDO Methods," SAE Paper 94-1165, April 1994.

[3] Perkins, H. D., Scott, R. T., and Pack, W. D., "Mach 5 to 7 RBCC Propulsion System Testing at NASA-Le RC HTF," NASA TM 107384; also AIAA Paper 97-0565, Jan. 1997.
[4] Youngster, S., and Trefny, C. J., "Analysis of a New Rocket-Based Combined-Cycle Concept at Low Speed," NASA TM 1999-209393, Sept. 1999.
[5] Siebenhaar, A., Bulman, M. J., and Bonnar, D. K., "Strutjet Rocket-Based Combined-Cycle Engine," *Scramjet Propulsion*, Vol. 189, Progress in Astronautics and Aeronautics, AIAA, Reston, VA, 2000, pp. 697–755.
[6] Olds, J., and Bradford, J. E., "SCCREAM: A Conceptual Rocket-Based Combined-Cycle Engine Performance Analysis Tool," *Journal of Propulsion and Power*, Vol. 17, No. 2, 2001, pp. 333–339.
[7] Kanda, T., and Kudo, K., "Conceptual Study of a Combined-Cycle Engine for an Aerospace Plane," *Journal of Propulsion and Power*, Vol. 19, No. 5, 2003, pp. 859–867.
[8] Bertram, M. H., "Hypersonic Laminar Viscous Interaction Effects on the Aerodynamics of Two-Dimensional Wedge and Triangular Platform Wings," NASA, TN D-3523, Langley Research Center, Hampton, VA, Aug. 1966.
[9] Anderson, J. D., Jr., "Hypersonic Viscous Interaction," *Hypersonic and High-Temperature Gas Dynamics*, edited by J. A. Schetz, 2nd ed., AIAA Education Series, AIAA, Reston, VA, 2006, pp. 375–413.
[10] Kubota, S., Tani, K., and Masuya, G., "Aerodynamic Performances of a Combined Cycle Inlet," *Journal of Propulsion and Power*, Vol. 22, No. 4, 2006, pp. 900–904.
[11] Tani, K., Kanda, T., and Kudou, K., "Aerodynamic Performance of Scramjet Inlet Models with a Single Strut," *Journal of Propulsion and Power*, Vol. 22, No. 4, 2006, pp. 905–912.
[12] Hiraiwa, T., Kanda, T., Kobayashi, K., and Saito, T., "Experiments on Scramjet Engine with Ramp-Compression Inlet at Mach 8," *Journal of Propulsion and Power*, Vol. 22, No. 2, 2006, pp. 440–446.
[13] Riva, G., Reggiori, A., and Daminelli, G., "A New Pulse Facility for Studies on Rocket-Based Combined Cycles," *Space Technology*, Vol. 25, No. 2, 2005, pp. 83–92.
[14] Heiser, W. H., and Pratt, D. T., "Compression Systems or Components," *Hypersonic Airbreathing Propulsion*, edited by J. S. Przemieniecki, AIAA Education Series, AIAA, Washington, D.C., 1994, pp. 197–275.
[15] Houghton, E. L., and A. E. Brock, A. E., *Tables for the Compressible Flow of Dry Air*, 3rd ed., Edward Arnold Ltd., London, 1975.
[16] Van Wie, D., "Scramjet Inlets," *Scramjet Propulsion*, edited by P. Zarchan, Vol. 189, Progress in Astronautics and Aeronautics, AIAA, Reston, VA, 2000, pp. 447–511.

T. Wang
Associate Editor